

# How Nanopore Translocation Experiments Can Measure RNA Unfolding

Prasad Bandarkar,<sup>1</sup> Huan Yang,<sup>1</sup> Robert. Y. Henley,<sup>2</sup> Meni Wanunu,<sup>1,\*</sup> and Paul C. Whitford<sup>1,\*</sup>

<sup>1</sup>Department of Physics, Northeastern University, Boston, Massachusetts and <sup>2</sup>Genomic Analysis Laboratory, The Salk Institute for Biological Studies, La Jolla, California

**ABSTRACT** Electrokinetic translocation of biomolecules through solid-state nanopores represents a label-free single-molecule technique that may be used to measure biomolecular structure and dynamics. Recent investigations have attempted to distinguish individual transfer RNA (tRNA) species based on the associated pore translocation times, ion-current noise, and blockage currents. By manufacturing sufficiently smaller pores, each tRNA is required to undergo a deformation to translocate. Accordingly, differences in nanopore translocation times and distributions may be used to infer the mechanical properties of individual tRNA molecules. To bridge our understanding of tRNA structural dynamics and nanopore measurements, we apply molecular dynamics simulations using a simplified “structure-based” energetic model. Calculating the free-energy landscape for distinct tRNA species implicates transient unfolding of the terminal RNA helix during nanopore translocation. This provides a structural and energetic framework for interpreting current experiments, which can aid the design of methods for identifying macromolecules using nanopores.

**SIGNIFICANCE** This study employs simulations to explore the structural characteristics that govern transport of transfer RNA through a nanopore. By adopting a simplified description, the presented calculations demonstrate that the energetics of transfer RNA folding can rationalize the differential translocation timescales that have been observed in experiments. Through comparison with experimental measurements, the presented calculations provide a physical and chemical foundation that can enable nanopore technologies to measure the stabilities of RNA helices.

## INTRODUCTION

Advances in nanopore fabrication and design (1–5) provide a range of new opportunities to probe the physical characteristics of biomolecules. In nanopore experiments, a dielectric membrane with a single nanopore separates two electrodes in an electrolytic cell, and charged biomolecules are introduced into one of the chambers. When a voltage is applied between the electrodes, the flow of ions results in a constant “open-pore” current. However, when a biomolecule reaches the pore opening, the flow of ions is partially (or fully) obstructed. This results in a net reduction of the current flow, where the duration and current level depends on the properties of the biomolecule. To quantify blockage dynamics, the most commonly employed metrics are the magnitude ( $\Delta I$ ) and duration (dwell time,  $t_d$ ) of the current drop. Because

these quantities are sensitive to the precise physical attributes of the pore-biomolecule complex, the statistical properties of blockage distributions will encode signatures of the biomolecular dynamics.

Quantifying transport through nanopores has the potential to provide insights into the physical properties that govern functional dynamics of biomolecules, such as proteins (6–10) and transfer RNA (tRNA) (11,12). During protein synthesis in the cell, codon-anticodon interactions are formed between tRNA and messenger RNA, which allow the ribosome to accurately decode messenger RNA sequences. Because the energetic differences between correct and incorrect tRNA basepairing can only partially account for the fidelity of translation, the ribosome employs a subsequent proofreading step (13–15). This involves a large-scale conformational change (i.e., accommodation) in the incoming tRNA molecule, during which intramolecular tRNA interactions that are distal to the anticodon region can modulate the accuracy of translation (16). Subsequent to accommodation, tRNA molecules must undergo several

Submitted August 22, 2019, and accepted for publication January 30, 2020.

\*Correspondence: [m.wanunu@northeastern.edu](mailto:m.wanunu@northeastern.edu) or [p.whitford@neu.edu](mailto:p.whitford@neu.edu)

Editor: Wilma Olson.

<https://doi.org/10.1016/j.bpj.2020.01.030>

© 2020 Biophysical Society.

additional rearrangements to complete the elongation cycle (17–20), and a balance between ribosome and tRNA flexibility is necessary to ensure rapid dynamics (21–23). With the essential role of molecular flexibility during protein synthesis, measuring the mechanical properties of tRNA can help reveal principles that underlie accurate gene expression. Accordingly, this class of molecules represents an excellent test case for the application of nanopore-based measures of molecular flexibility, in which physical insights can have biological implications.

In recent nanopore translocation experiments, it was shown that current signals for different tRNA species are sufficiently distinct to differentiate the tRNA species. By combining the signals with machine-learning algorithms, the identity of one type of tRNA in a binary mixture could also be discerned from a single-molecule pulse (12). In those experiments, the width of the nanopore was chosen to be larger than the radius of an RNA double helix, although it was also sufficiently small that tRNA is unable to translocate without undergoing a deformation (Fig. 1). The motivation for the measurement was, due to the fact that the molecule must rearrange to translocate, it could be possible to use nanopores to measure molecular flexibility. These early experiments demonstrated a potential for nanopores to elucidate the mechanical properties of RNA, where future objectives may include the characterization of mutations, as well as post-transcriptional modifications. However, even though structural data suggest qualitative mechanistic interpretations, establishing a quantitative relationship between current changes and biomole-

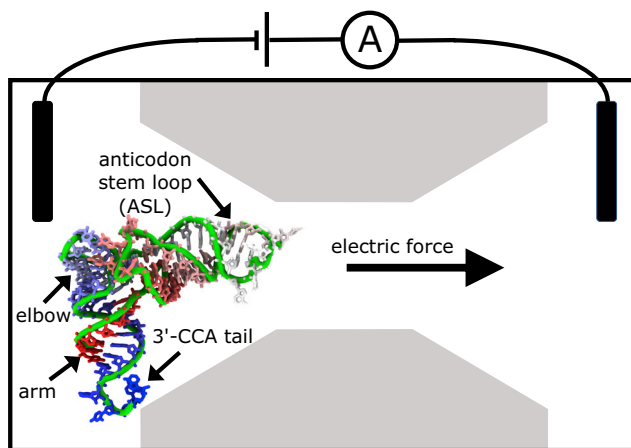


FIGURE 1 Schematic representation of a tRNA-nanopore experiment. A dielectric membrane (gray) separates the electrolytic cell into two chambers, and solvent is allowed to pass through a nanometer-scale pore. The geometry of a nanopore typically consists of conical openings connected by a cylindrical region. Here, the diameter of the cylinder is drawn to scale, relative to the dimensions of a tRNA molecule. Because of the L-shaped structure of a tRNA molecule, translocation through a nanopore requires molecular deformations, which may involve a range of distortions. The detailed character of these deformations will govern the measured changes in ion currents. To see this figure in color, go online.

cular properties will require a more comprehensive physical-chemical framework. It is our expectation that a detailed understanding of this relationship may allow next-generation nanopore measurements to provide precise insights into biologically relevant molecular properties.

In our study, we employ molecular dynamics (MD) simulations with a simplified model of tRNA to explore the relationship between structural dynamics and nanopore translocation kinetics. Here, we describe the internal energetics of the tRNA molecule using a force field in which all nonhydrogen atoms are represented and the native conformation is explicitly defined to be stable (i.e., an all-atom structure-based model (24,25)). To mimic the pore, we account for excluded volume interactions between the pore and tRNA, and electrophoretic effects are treated through perturbative techniques. Although this is intended to be a simplified representation, we find that it is sufficient to capture the experimentally observed differential kinetics of tRNA species. Contrary to expectations, this analysis also indicates that the translocation process is not associated with simple bending and shearing motions of the tRNA. Rather, there is a dramatic unfolding of the tRNA acceptor arm helix. Taken together, these results illustrate how current nanopore technologies may be combined with molecular simulations to measure the stabilities of individual helices within RNA assemblies.

## METHODS

### RNA force field

An all-atom structure-based model (24) was used to describe the intramolecular energetics of the tRNA molecule. This model was generated using the SMOG-server webtool (25). In this model, all heavy (nonhydrogen) atoms are represented as spheres of unit mass. The functional form of the potential is given by

$$\begin{aligned}
 V = & \sum_{\text{bonds}} \epsilon_r (r - r_0)^2 + \sum_{\text{angles}} \epsilon_\theta (\theta - \theta_0)^2 \\
 & + \sum_{\text{improper and}} \epsilon_\chi (\chi - \chi_0)^2 + \sum_{\text{flexible dihedrals}} \epsilon_\phi F(\phi, \phi_0) \\
 & + \sum_{\text{planar dihedrals}} \epsilon_c \left[ \left( \frac{\sigma_{ij}}{r_{ij}} \right)^{12} - 2 \left( \frac{\sigma_{ij}}{r_{ij}} \right)^6 \right] + \sum_{\text{non-contacts}} \epsilon_{nc} \left( \frac{\sigma_{NC}}{r_{ij}} \right)^{12}
 \end{aligned} \quad (1)$$

where

$$F(\phi, \phi_0) = [1 - \cos(\phi - \phi_0)] + \frac{1}{2} [1 - \cos(3(\phi - \phi_0))]. \quad (2)$$

The parameters  $\{r_0\}$ ,  $\{\theta_0\}$ ,  $\{\chi_0\}$ ,  $\{\phi_0\}$ , and  $\{\sigma_{ij}\}$  are given the values adopted in the crystallographic structure of each molecule. Thus, the potential energy is defined to have a global minimum that corresponds to the

crystallographic structure. We use a reduced energy scale in units of  $\epsilon_0 = 1$  for all terms. As described below, free-energy profiles were calculated at a reduced temperature of 0.71. Accordingly,  $\epsilon_0 = (k_B T / 0.71) = 1.42 k_B T$ . Consistent with previous implementations, the coefficients for this model are given the values  $\epsilon_r = 50\epsilon_0/\text{nm}^2$ ,  $\epsilon_\theta = 40\epsilon_0/\text{rad}^2$ ,  $\epsilon_{\chi\text{improper}} = 10\epsilon_0/\text{rad}^2$ ,  $\epsilon_{\chi\text{planar}} = 40\epsilon_0/\text{rad}^2$ ,  $\epsilon_{\text{NC}} = 0.01 \epsilon_0$  and  $\sigma_{\text{NC}} = 2.5\text{\AA}$ . To assign the dihedral strengths, the number of dihedral angles that share a pair of atoms is determined. If  $N_D$  is the number of dihedrals that share a center bond, the energy of each such dihedral angle is scaled by  $1/N_D$ . The weights of the dihedral and contact energies are set such that

$$\frac{\sum \epsilon_c}{\sum \epsilon_\phi} = 2 \quad (3)$$

and

$$\sum \epsilon_c + \sum \epsilon_\phi = N\epsilon_0,$$

where  $N$  is the number of atoms in the molecule.

As seen in the functional form of the potential, all the interactions (except for noncontacts) stabilize the crystallographic structure of the molecule. By defining an experimental structure as stable, the direct interactions in this model describe the effective energetics of the system. That is, each stabilizing nonbonded term implicitly accounts for the stability imparted by nonspecific electrostatic and solvent interactions. The noncontacting atom pairs are given excluded volume interactions, which ensure that proper stereochemistry is preserved. The structures were obtained from Protein Data Bank entries 1F7U (26) for tRNA<sup>Arg</sup>, 1QU3 (27) for tRNA<sup>Ile</sup>, and 1EHZ (28) for tRNA<sup>Phe</sup>.

## tRNA-pore interaction

In the presented model, the tRNA only interacts with the pore through an excluded volume interaction:

$$V_{\text{pore}} = \sum_{\text{all atoms}} \epsilon_{\text{pore}} \left( \frac{\sigma_{\text{pore}}}{r} \right)^{12}, \quad (4)$$

where  $\epsilon_{\text{pore}} = \epsilon_{\text{NC}} = 0.01\epsilon_0$ ,  $\sigma_{\text{pore}} = \sigma_{\text{NC}} = 2.5\text{\AA}$ , and  $r$  is the shortest distance between each atom and the pore wall.

The pore is defined as a long cylinder of radius  $r_{\text{pore}}$  with a conical mouth followed by a flat wall perpendicular to the axis of the pore (Fig. 1). Because of the excluded volume interaction of the pore, the effective radius of the pore is  $r_{\text{pore}} - \sigma_{\text{pore}}$ . This pore geometry is consistent with the observed geometry (29) of the solid-state nanopores used in the experimental study of tRNA (12).

## Simulation details

Umbrella sampling (30) was used in conjunction with replica exchange protocols (31,32) to calculate the free energy as a function of the tRNA position. Each umbrella was included as a harmonic restraint along  $I$  (coordinate of the center of mass of 41 residues that are near the anticodon stem-loop (ASL); Fig. 1). Umbrellas were defined from  $I = -18\text{nm}$  to  $I = 10\text{ nm}$  spaced at 0.2-nm intervals. Initially, short equilibration simulations were iteratively performed: the model was initially equilibrated at  $I = -3\text{ nm}$ . The equilibrated structure was then used to initiate the  $I = -2.8\text{ nm}$  and the  $I = -3.2\text{ nm}$  runs. This was repeated until  $I = 10\text{ nm}$  (inside the pore) and  $I = -18.0\text{nm}$  (outside the pore) were reached. The system was initially positioned such that the ASL loop was inserted in the pore. After an initial equilibration period, replica exchange simulations with 10 temperatures were performed for each value of the umbrella position. No electrophoretic bias was applied during the simulations. These

simulations were repeated for pores of radii 3.5, 3.8, and 4 nm for tRNA<sup>Arg</sup> and tRNA<sup>Ile</sup>. The simulations were performed using Gromacs (version 4.6.7) (33) with in-house source-code modifications added to include the pore-tRNA interactions. Reduced units were utilized for all calculations. The iterative equilibration runs were each performed for 500,000 steps of size 0.002, whereas the replica exchange runs were performed for at least 80 million steps. Comparison of tRNA dynamics with an SMOG model and an explicit-solvent model suggests the effective reduced timescale is between 50 ps and 1 ns (34). Accordingly, one may estimate the effective simulated time of each replica to be  $\sim 50\text{--}100\text{ }\mu\text{s}$ . For replica exchange simulations, temperatures between 0.71 and 0.89 were chosen with geometric spacing, in order to obtain an exchange acceptance probability of  $\sim 0.2$ . Langevin dynamics protocols with the leap-frog integrator were applied to maintain a constant temperature. All reported quantities were obtained for the lowest simulated temperature of 0.71 (reduced units). In this model, tRNA structure is found to melt at around 0.9 reduced units (data not shown). tRNA molecules tend to denature around 350 K (35). Accordingly, the simulated temperatures may be estimated as ranging from 280 to 350 K.

The weighted histogram analysis method (WHAM) (36) was used to calculate free-energy profiles from the umbrella simulations. To verify convergence of the free-energy profiles, WHAM calculations were repeated using the first or second half of the simulated time (Fig. S1) To account for the electrophoretic bias along the pore, we assume a uniform electric potential gradient that is parallel to the axis of the pore. The electric potential decreases linearly from  $V_{\text{applied}}$  to zero over a distance of 30 nm ( $I = -10\text{ nm}$  to  $I = 20\text{ nm}$ ). To implement a reduced effective charge due to solvation of phosphate groups, each phosphorous atom was modeled as carrying an effective charge of  $-\theta_c$ , for which the precise value in each calculation was held at a specific uniform value. Different calculations used distinct values that ranged from 0 to 1.  $\theta_c = 1$  would correspond to the case in which there is no counterion condensation. The average electrophoretic potential energy of the tRNA was calculated post hoc as a function of the translocation coordinate ( $I$ ), based on the simulated positions of the P atoms. That is, the electrophoretic potential profile was added to the free-energy profile obtained from WHAM to provide an effective free-energy profile as a function of  $I$ . Here, directly adding the potential energy is a suitable approximation because the variation in electric potential energy (for a given value of  $I$ ) was small ( $< 1k_B T$ ) relative to the change in potential energy during translocation ( $\approx 100k_B T$ ).

## RESULTS AND DISCUSSION

To identify the molecular factors that lead to differential kinetics of tRNA translocation through nanopores, we constructed a simplified energetic model and then used MD simulations to calculate the free-energy barriers associated with tRNA translocation events. Specifically, we utilized an all-atom structure-based model (24,25) in which all interactions were explicitly defined to stabilize an experimentally-resolved structure. This model was chosen because it provides a description of molecular flexibility that is consistent with more highly detailed models (37) and crystallographic B-factors (38). To model the presence of the nanopore, we introduced repulsive interactions between the tRNA and pore, where the pore was described as a cylindrical surface with a conical opening (Fig. 1). By defining the tRNA-pore interactions as purely repulsive, this model is designed to identify the extent to which confinement of tRNA leads to specific structural deformations during translocation. That is, by using a model that provides a description of flexibility that is consistent with

other theoretical and experimental measures, the objective is to determine whether molecular flexibility is sufficient to rationalize the translocation kinetics. As described below, we find that flexibility is not sufficient, and more dramatic unfolding processes are likely to occur. Because the modeled flexibility and sterics of confinement are consistent with more highly detailed models, one further expects that partial unfolding will be a robust feature when using other models. To assess whether the predicted kinetics are quantitatively consistent with experimental measurements, we used perturbation techniques to describe the effects of electrophoretic bias, counterion condensation, and hydrodynamic drag. When accounting for these factors, the simplified representation of tRNA-pore energetics is sufficient to rationalize the differential translocation kinetics of tRNA<sup>Ile</sup> and tRNA<sup>Arg</sup>. From a mechanistic perspective, these calculations implicate partial unfolding as the key molecular process that determines translocation kinetics.

### Simplified molecular model captures translocation kinetics

To determine whether the simplified model is able to account for differential tRNA kinetics, we first calculated the free-energy barriers of translocation in the absence of an electrophoretic bias. After calculating the field-free barriers, we then introduced the electrophoretic effects to calculate perturbed free-energy surfaces. To illustrate the overall approach, we first provide a description for tRNA<sup>Arg</sup>. In the simulations, intramolecular tRNA interactions are explicitly defined to stabilize the folded conformation, whereas the tRNA and pore only interact through a repulsive potential. It should be noted that nitride pores can form nonspecific stabilizing interactions with tRNA, which can introduce an overall drag on the molecule (39,40). As described below, in our study, we account for drag implicitly using a perturbative approach. Umbrella sampling and replica exchange techniques were applied to calculate the free energy as a function of tRNA position within the pore (see Methods for simulation details). The corresponding rates of pore translocation were then obtained by describing tRNA motion in terms of diffusion along a one-dimensional free-energy surface. Specifically, we calculated the free energy as a function of the axial position ( $I$ ) of the ASL (Fig. 2 a, green). By describing the motion in terms of diffusion across a one-dimensional free-energy surface  $G(I)$ , the corresponding mean first-passage time (MFPT) may be calculated according to (41,42)

$$\text{MFPT} = \int_{I_{\text{init}}}^{I_f} dI \int_{-\infty}^I dI' \frac{\exp[(G(I) - G(I'))/k_B T]}{D_I^{\text{eff}}(I')}, \quad (5)$$

where  $I_{\text{init}}$  corresponds to the position of the free-energy minimum that is encountered immediately before crossing the barrier (i.e., post-capture, pretranslocation) and  $I_f$  corre-

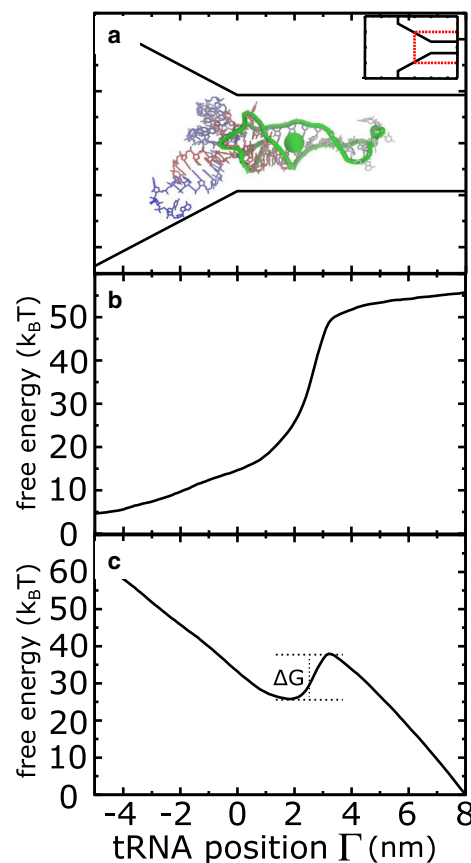


FIGURE 2 Modeled pore geometry and calculated free-energy profiles. (a) Schematic representation of a 3.7-nm diameter pore (full pore dimensions shown in inset) is shown. tRNA<sup>Arg</sup> is shown to scale. Here, translocation through the pore is described by the coordinate  $I$ : axial position of the center of mass of the residues near the anticodon stem-loop (ASL) region. The ASL region used for center-of-mass calculations is shown in green tubes, and the position of the center of mass is depicted by the green sphere. (b) The free-energy profile in the absence of an applied electric field is shown. As expected, there is a large ( $>50k_B T$ ) barrier, which is consistent with a lack of observed translocation events in the absence of an applied field (46). (c) The free-energy profile obtained after including the effect of an external potential with a strength of 200 mV is shown. Under these conditions, the predicted free-energy barrier  $\Delta G$  is  $\sim 12k_B T$ . To see this figure in color, go online.

sponds to the value of the same coordinate when the entire molecule is inside the pore. Numerically,  $I_{\text{init}} \approx 2$  nm and  $I_f = 7$  nm (Fig. 2). Although it is possible that the diffusion of tRNA molecules in nanopores will be position dependent, as observed in protein-folding studies (43), for simplicity, we apply a constant value based on the Stokes-Einstein estimates ( $100 \mu\text{m}^2/\text{s}$  for a radius of gyration of  $\sim 2.3$  nm). Consistent with this estimate, proteins of similar radii of gyration have been observed to show comparable diffusion constants in vitro (44,45).

As expected, in the absence of an electric field, there is a large ( $>50k_B T$ ) free-energy barrier (Fig. 2 b). A barrier of this magnitude would correspond to negligibly slow kinetics, which is consistent with a lack of observed

translocation events in the absence of a significant electrophoretic bias (46).

To calculate the rate of translocation as a function of applied field strength, we used our field-free simulations and employed a perturbation approach. The average electrostatic potential energy was calculated as a function of the progress coordinate  $T$  and then added to the unperturbed free-energy profile. For these calculations, the field was modeled as being a uniform strength between the openings of the conical mouth of the pore (linearly decreasing potential from the value  $V_{\text{applied}}$  to zero over a distance of 30 nm along the axis of the pore), and each backbone phosphorous atom was assigned a charge of  $-e$ . Intra-tRNA electrostatic interactions were not considered because these are implicitly described in structure-based models (47). To account for the influence of counterion condensation and drag on the tRNA, we further rescaled the effective charge of each residue by the factor  $\theta_c$ . Although an exact value of  $\theta_c$  is not currently known, direct force measurements have estimated it to be  $\sim 0.25\text{--}0.35$  for double-stranded DNA in the presence of a nanopore (48). However, it is worth noting that Ghosal (49) showed the effective rescaling of electrophoretic forces may primarily arise from hydrodynamic drag effects. Luan et al. (39,40) came to the same conclusion by observing a pore-size dependence on the radial ion distribution in MD simulations. In this study, we do not distinguish between these possible contributions. Rather, we use these empirical measurements and predicted values to guide the approximate scale of  $\theta_c$  in our calculations. For values of  $\theta_c$  ranging from 0.25 to 0.40, we added the effective electrostatic energy to the unbiased free-energy profile to estimate the field-dependent free-energy profile along  $T$ .

Consistent with experimental observations, we find that the free-energy barrier and MFPT decrease with increasing electrophoretic bias (Fig. 3). At low-field strengths, the MFPT decreases with electrophoretic bias. However, at high-applied voltages, the scale of the electrophoretic bias

greatly exceeds the sterically induced barrier, which leads to a downhill free-energy profile (Fig. S2). As a result, the MFPT becomes saturated and appears to adopt a diffusion-limited value.

Although the presented model provides a simplified representation of the system, the predicted kinetics are on the same scale as those obtained experimentally (Fig. 3; (12)). When accounting for the uncertainty in the condensation factor  $\theta_c$ , the predicted range of rates includes the experimental values for the applied voltage that span from 200 to 400 mV for both tRNA<sup>Arg</sup> and tRNA<sup>Ile</sup>. We also find that tRNA<sup>Phe</sup> is slower than tRNA<sup>Ile</sup> (Figs. S3 and S4). The displayed level of agreement indicates that native interactions and excluded volume effects are sufficient to provide a rough estimate of the translocation rates. It is also interesting that the free-energy barriers reported here are similar to the predicted internal energy of tRNA<sup>Phe</sup> bending (50), which was based on an adiabatic mapping technique. Although the range of predicted timescales is somewhat broad, the uncertainty in  $\theta_c$  only introduces an uncertainty of  $\pm 5k_B T$  in the free-energy barrier height. When considering the various unquantified experimental factors (pore asymmetry, nonuniform field effects, etc.), it is nontrivial to obtain barriers that are consistent with experiments to within a few  $k_B T$ . This degree of similarity is even more surprising when one considers that the effective free-energy profiles result from the contributions of multiple large ( $\sim 50\text{--}100k_B T$ ) quantities (i.e., initial free-energy barrier and electrophoretic effects). If the molecular model, or the modeled electrophoretic effects, were sufficiently imprecise, then the predicted timescales could easily differ from experiments by many orders of magnitude. Here, we consider the case in which the tRNA anticodon region enters the pore first. This simplification is motivated by the observation that the flexibility of the 3'-CCA is much larger than that of the anticodon region, as measured by the root mean-square fluctuations (RMSFs) (Fig. S5). Accordingly, this

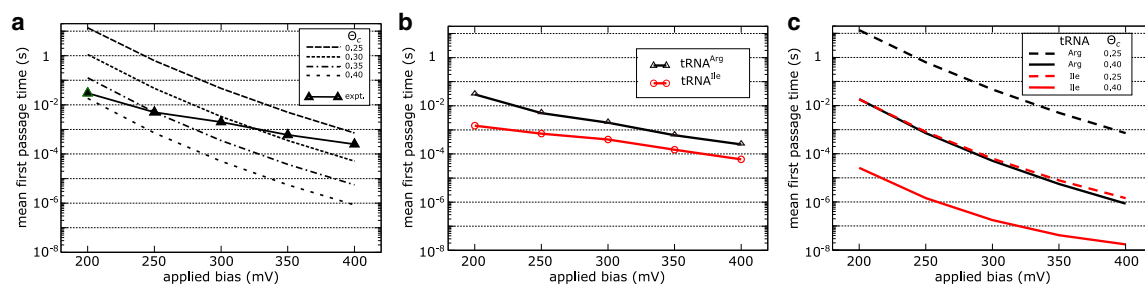


FIGURE 3 Predicted mean first-passage times (MFPTs) are comparable to experimental dwell times. (a) The MFPTs predicted for tRNA<sup>Arg</sup> as a function of applied field strength for different values of the ion condensation factor  $\theta_c$  (dashed lines) are shown. The experimentally measured dwell times are within the range of the predicted values, which illustrates how a simple energetic model can predict an overall timescale that is consistent with experimental measurements. (b) Experimental dwell times for tRNA<sup>Arg</sup> and tRNA<sup>Ile</sup> show a distinct separation in which shorter dwell times are associated with tRNA<sup>Ile</sup>. This separation in timescales is consistent with previous experimental measurements (12). Here, to reduce the influence of pore heterogeneity, measurements were taken for both species using the same physical pore. (c) Theoretical MFPTs for tRNA<sup>Arg</sup> and tRNA<sup>Ile</sup> ( $\theta_c = 0.25$  and 0.40 shown) also predict faster kinetics are associated with tRNA<sup>Ile</sup>. Overall, the structure-based model identifies differential kinetics and timescales that are similar to experiments. To see this figure in color, go online.

difference in flexibility should disfavor initial capture of the 3'-CCA end. Although it is possible that the tRNA may enter via the 3'-CCA end, our study shows that capture via the anticodon region is sufficient to rationalize the experimental differences in rates. However, it is worth noting that because the in-pore ensemble was exhaustively sampled, the structural properties of the tRNA inside of the pore (described below) will not depend on the direction of entry. With these limitations in mind, this comparison indicates that the model provides a physical-chemical description of the mechanical properties of tRNA that is consistent with experimentally measured kinetics.

In addition to providing a predicted translocation time-scale for tRNA<sup>Arg</sup> that is similar to experimental values, this model also predicts faster rates for tRNA<sup>Ile</sup> (Fig. 3 c). The predicted rates for tRNA<sup>Arg</sup> are consistently lower than for tRNA<sup>Ile</sup>, regardless of the precise pore size used in the calculations (Fig. S6). Furthermore, we find that the separation of rates is robust to changes in the simulated temperature (Fig. S7). The robustness of these trends supports the use of simplified structure-based models to identify mechanistic features that can rationalize experimentally observed differences in kinetics.

### Partial unfolding of the tRNA is associated with translocation

One can envision a variety of mechanistic scenarios that could explain the apparent free-energy barriers associated with translocation. Translocation could involve bending and/or shearing motions that allow the molecule to preserve the majority of the secondary and tertiary interactions. A more drastic process could involve loss of some or all of the tertiary and/or secondary structure interactions. This would result in an unfolded chain that exhibits significant disorder in the backbone. However, pore-induced confinement should disfavor an extended unfolded ensemble (51–54). With this range of mechanistic possibilities, simulations provide an opportunity to identify which of these possess physical-chemical properties that are compatible with experimentally measured kinetics.

To probe whether unfolding or melting is associated with translocation, we calculated the fraction of native contacts formed per residue ( $Q_i$ ) as a function of the translocation coordinate  $\Gamma$ . Here, native contacts are defined as nonbonded interactions present in the native structure of the tRNA, as identified by the Shadow algorithm (55). Consistent with studies of protein folding, for a given simulated configuration, a native contact is considered to be “formed” if the respective atom pair is within 1.2 times the native distance (24,25,56). We further partition the native contacts into stacking and nonstacking (e.g., basepairing and tertiary) interactions. We find that the average fraction of nonstacking native interactions decreases as the tRNA molecule enters the pore (Fig. 4, a and c). Specifically, there is a decrease

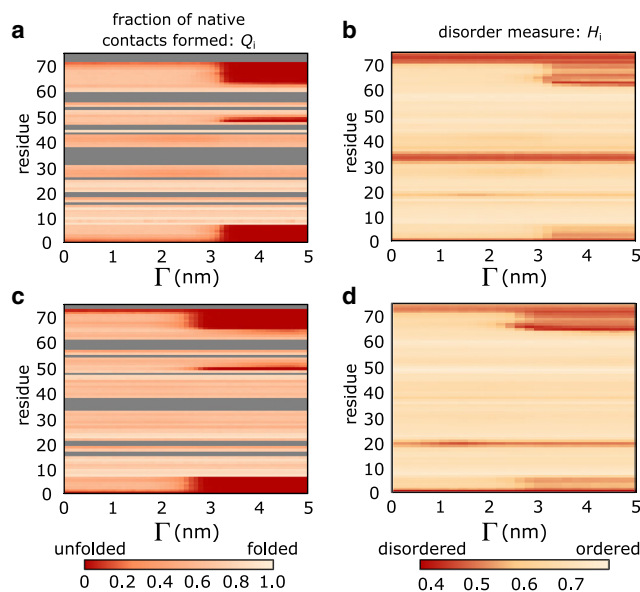


FIGURE 4 Pore entry leads to tRNA unfolding. (a) Average fraction of native contacts formed per residue  $Q_i$ , as a function of tRNA translocation, for tRNA<sup>Arg</sup>. Gray indicates that a residue does not have any contacts in the native structure. As the tRNA molecule initially enters the pore ( $\Gamma \sim 3$  nm), there is a sharp decrease in the fraction of native contacts formed ( $\sim 0.9$  to  $\sim 0.2$ ) in the acceptor arm and 3'-CCA end (Fig. 1). (b) The average Hellinger distance per residue ( $H_i$ ), as a function of the translocation coordinate  $\Gamma$ , for tRNA<sup>Arg</sup>. There is an abrupt decrease in  $H_i$  (from  $\sim 0.7$  to  $\sim 0.4$ ) for acceptor arm residues, which signifies an increase in disorder of the tRNA backbone. Similarly,  $Q_i$  and  $H_i$  calculated for tRNA<sup>Ile</sup> (c and d) confirm that a decrease in native content and an increase in disorder are associated with nanopore translocation for both molecules. To see this figure in color, go online.

in the fraction of contacts formed in the acceptor arm region (residues 1–7, 50, 66–73; Fig. S8) at  $\Gamma \approx 2$ –3 nm. There is also a concomitant decrease in the fraction of stacking contact pairs in these residues (Fig. S9). The remaining residues do not display a significant reduction in  $Q_i$ , indicating that overcoming the free-energy barrier is primarily associated with changes in the acceptor stem.

Because the loss of the native structure would suggest the tRNA molecule unfolds upon entry into the pore, we next asked whether there is also a substantial increase in the degree of disorder of the molecule. To address this, we calculated the Hellinger distance between the distribution of each backbone dihedral angle and a uniform distribution. The Hellinger distance is a measure of similarity between two probability distributions, and it is defined as follows (57):

$$H = \frac{1}{\sqrt{2}} \sqrt{\sum_{j=1}^k (\sqrt{p_j} - \sqrt{q_j})^2}, \quad (6)$$

where  $P = (p_1, \dots, p_k)$  and  $Q = (q_1, \dots, q_k)$  are any two discretized and normalized probability distributions.  $H = 0$  for identical distributions, and  $0 < H \leq 1$  if there are differences, with larger values indicating more significant

differences in the distributions. Here, we compare the probability distribution of an individual dihedral angle ( $P$ ) against a uniform distribution ( $Q$ ). A uniform distribution is used for comparison because it would represent a perfectly disordered dihedral angle. With this definition,  $H$  will be proportional to the degree of order in an individual dihedral. For reference, representative distributions for  $H \sim 0.3$  and  $H \sim 0.8$  are shown in Fig. S11.

We find that upon tRNA entry into the pore, an increase in disorder coincides with a loss of secondary structure (Fig. 4). Specifically, there are sharp decreases in the average value of  $H$  for specific residues ( $H_i$ : average value of  $H$  for dihedrals in a residue) upon entry (Fig. 4, *b* and *d*). Although the RNA backbone is well ordered before entering the pore ( $H_i \sim 0.7$  for most residues), the loss of native contacts leads to the tRNA arm becoming locally disordered ( $H_i \sim 0.4$ ), even in this confined environment. These low values of  $H_i$  are comparable to the values found for the single-stranded 3'-CCA end (residues 74–76), which has previously been described as a highly disordered/unfolded region (58). Together, this analysis reveals that the acceptor arm does not simply deform, but it enters a disordered ensemble of unfolded configurations during the translocation process. With regards to the dynamics of other tRNA types, the current results suggest that if a tRNA molecule favors a larger angle between the acceptor arm and ASL (e.g., mitochondrial tRNA) or if the acceptor arm is less stable, one should observe faster nanopore translocation kinetics.

### Unfolding and confinement lead to nonmonotonic changes in configurational entropy

One implied consequence of the presented calculations is that capture rates and translocation rates will have opposing temperature dependencies. To better understand the potential temperature dependence, it is instructive to consider the configurational entropy as a function of tRNA displacement. Before discussing the results, it is important to note that these calculations only describe the configurational entropy of the tRNA molecule. Accordingly, one should not compare the precise values to experimental quantities, which will necessarily depend on the solvent. From our simulations, we calculated the configurational entropy as a function of tRNA position (Fig. 5 *a*) from the free energy and average energy according to the following equation:  $\Delta S(T) = (\langle \Delta E \rangle(T) - \Delta G(T))/T$ . We find that during initial association (i.e., capture) with the pore ( $-5 \text{ nm} < \Gamma < 0 \text{ nm}$ ), there is a marginal decrease in configurational entropy. This decrease may be largely attributed to a reduction of accessible rotational motion. To quantify the change in rotational motion upon entry into the pore, we calculated the orientational order parameter

$$m = \frac{3\cos^2\theta - 1}{2}. \quad (7)$$

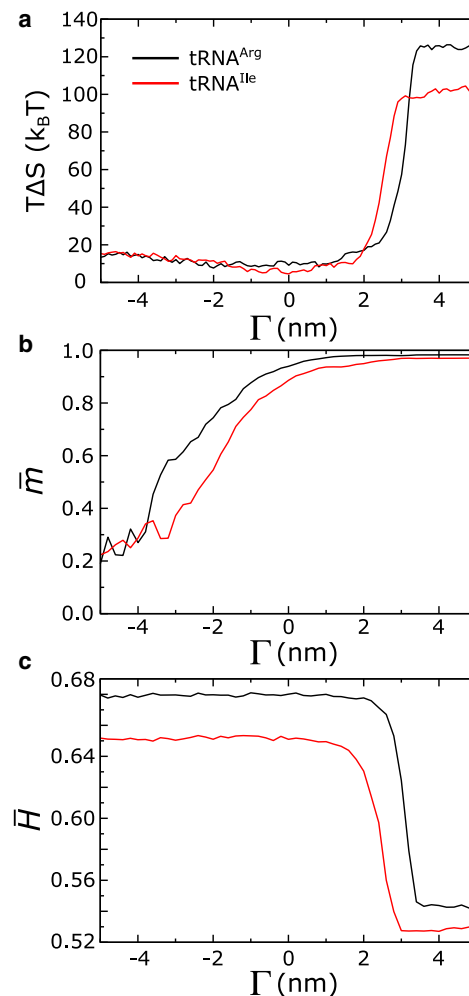


FIGURE 5 Nonmonotonic configurational entropy during translocation. (a) During the initial association with the pore ( $\Gamma < 0$ ), there is a modest decrease in configurational entropy, which is followed by a sharp increase during translocation ( $\Gamma > 0$ ). (b) The initial decrease in configurational entropy may be partially attributed to the reduction in accessible rotational motion, as measured by the orientational order parameter  $\bar{m}$ . (c) During translocation, the overall increase in biomolecular disorder, as measured by the average value of  $H$  for acceptor arm residues ( $H$ ), can rationalize the sharp increase in configurational entropy. This overall nonmonotonic behavior of  $\Delta S$  suggests that tRNA capture and translocation will have opposing dependencies on temperature. To see this figure in color, go online.

Here,  $\theta$  is the angle formed by the first principal axis (lowest moment of inertia, Fig. S12) with the pore axis. The average value of  $m$  as a function of the translocation coordinate ( $\bar{m}(\Gamma)$ ) displays an increase from  $\sim 0$  (isotropic) to  $\sim 1$  (co-linear) that coincides with a reduction in the configurational entropy (Figs. 5 *b* and S13). The variance of  $m$  also decreases as the tRNA approaches the pore, consistent with a unimodal distribution of  $m$  values (data not shown). After initial association with the pore ( $\Gamma \sim 0$ ), the tRNA molecule transiently samples a free-energy minimum (Fig. 2 *c*) before unfolding the terminal acceptor arm helix (Fig. 4, *b* and *d*).

As the acceptor arm unfolds, there is a decrease in the average value of  $H_i$  ( $H_i$  of arm residues decrease from  $>0.65$  to  $\sim 0.5$ ; residues 3–6, 66–69; tRNA<sup>Ile</sup>: residues 1–4, 65–68) (Figs. 5 c and S14), with individual values dropping by as much as 0.3 (Fig. S14). Together, the modest reduction in entropy during association would suggest that the rate of tRNA capture will be weakly dependent on temperature, whereas capture rates should decrease with increasing temperature. In contrast, the increase in entropy upon unfolding indicates that translocation rates should increase rapidly with temperature. We also note that the apparent change in configurational entropy is different for the two tRNA species (Fig. 5 a). This may be attributed to differences in stability of the acceptor arm helix when using this model. Specifically, because the RMSFs of the acceptor arm helix is larger for tRNA<sup>Ile</sup> than tRNA<sup>Arg</sup> when the molecules are folded (Fig. S5), there should be a smaller increase in entropy upon unfolding for tRNA<sup>Ile</sup>. This differential degree of flexibility is also supported by crystallographic B-factors, which implicate larger RMSF values for tRNA<sup>Ile</sup> (1.38 Å) than tRNA<sup>Arg</sup> (0.86 Å). Together, these observations demonstrate that the predicted temperature effects on translocation kinetics are generally in agreement with independent experimental observations.

## CONCLUSION

Nanofabrication technologies continue to be developed at a staggering rate. With the many possibilities for novel nanodevices, there is a growing need for quantitative descriptions of the underlying molecular processes that are being exploited. In the current study, we demonstrate how a relatively simple molecular model may be used to explore the origins of differential timescales of biomolecular transport through a nanopore. We find that tRNA transport is likely associated with the partial unfolding and melting of the tRNA structure. This suggests new strategies for designing nanotechnologies that can precisely measure the mechanical properties of individual biomolecules. Through the iterative development of theoretical models and experimental devices, it should soon be possible to design a range of nanotechnologies that can report on the precise properties of arbitrarily complex molecular systems.

## SUPPORTING MATERIAL

Supporting Material can be found online at <https://doi.org/10.1016/j.bpj.2020.01.030>.

## AUTHOR CONTRIBUTIONS

P.B. performed all production simulations. H.Y. performed preliminary simulations. R.H. performed the experiments and discussed results and analysis. All author prepared the manuscript.

## ACKNOWLEDGMENTS

We thank the Northeastern University Research Computing team and the Discovery Cluster for computational support.

This work was supported by the National Science Foundation (grant nos. MCB-1350312, MCB-1915843, and MCB-1645671).

## REFERENCES

1. Dekker, C. 2007. Solid-state nanopores. *Nat. Nanotechnol.* 2:209–215.
2. Venkatesan, B. M., and R. Bashir. 2011. Nanopore sensors for nucleic acid analysis. *Nat. Nanotechnol.* 6:615–624.
3. Miles, B. N., A. P. Ivanov, ..., J. B. Edel. 2013. Single molecule sensing with solid-state nanopores: novel materials, methods, and applications. *Chem. Soc. Rev.* 42:15–28.
4. Spitzberg, J. D., A. Zreben, ..., A. Meller. 2019. Plasmonic-nanopore biosensors for superior single-molecule detection. *Adv. Mater.* 31:e1900422.
5. Danda, G., and M. Drndić. 2019. Two-dimensional nanopores and nanoporous membranes for ion and molecule transport. *Curr. Opin. Biotechnol.* 55:124–133.
6. Cressiot, B., A. Oukhaled, ..., J. Pelta. 2012. Protein transport through a narrow solid-state nanopore at high voltage: experiments and theory. *ACS Nano.* 6:6236–6243.
7. Yusko, E. C., J. M. Johnson, ..., M. Mayer. 2011. Controlling protein translocation through nanopores with bio-inspired fluid walls. *Nat. Nanotechnol.* 6:253–260.
8. Larkin, J., R. Y. Henley, ..., M. Wanunu. 2014. High-bandwidth protein analysis using solid-state nanopores. *Biophys. J.* 106:696–704.
9. Waduge, P., R. Hu, ..., M. Wanunu. 2017. Nanopore-based measurements of protein size, fluctuations, and conformational changes. *ACS Nano.* 11:5706–5716.
10. Varongchayakul, N., J. Song, ..., M. W. Grinstaff. 2018. Single-molecule protein sensing in a nanopore: a tutorial. *Chem. Soc. Rev.* 47:8512–8524.
11. Wanunu, M., T. Dadosh, ..., M. Drndić. 2010. Rapid electronic detection of probe-specific microRNAs using thin nanopore sensors. *Nat. Nanotechnol.* 5:807–814.
12. Henley, R. Y., B. A. Ashcroft, ..., M. Wanunu. 2016. Electrophoretic deformation of individual transfer RNA molecules reveals their identity. *Nano Lett.* 16:138–144.
13. Thompson, R. C., and P. J. Stone. 1977. Proofreading of the codon-anticodon interaction on ribosomes. *Proc. Natl. Acad. Sci. USA.* 74:198–202.
14. Ruusala, T., M. Ehrenberg, and C. G. Kurland. 1982. Is there proofreading during polypeptide synthesis? *EMBO J.* 1:741–745.
15. Pape, T., W. Wintermeyer, and M. Rodnina. 1999. Induced fit in initial selection and proofreading of aminoacyl-tRNA on the ribosome. *EMBO J.* 18:3800–3807.
16. Cochella, L., and R. Green. 2005. An active role for tRNA in decoding beyond codon:anticodon pairing. *Science.* 308:1178–1180.
17. Yarus, M., M. Valle, and J. Frank. 2003. A twisted tRNA intermediate sets the threshold for decoding. *RNA.* 9:384–385.
18. Schmeing, T. M., and V. Ramakrishnan. 2009. What recent ribosome structures have revealed about the mechanism of translation. *Nature.* 461:1234–1242.
19. Korostelev, A., and H. F. Noller. 2007. The ribosome in focus: new structures bring new insights. *Trends Biochem. Sci.* 32:434–441.
20. Frank, J., and C. Spahn. 2006. The ribosome and the mechanism of protein synthesis. *Rep. Prog. Phys.* 69:1383–1417.
21. Nguyen, K., and P. C. Whitford. 2016. Steric interactions lead to collective tilting motion in the ribosome during mRNA-tRNA translocation. *Nat. Commun.* 7:10586.

22. Yang, H., J. K. Noel, and P. C. Whitford. 2017. Anisotropic fluctuations in the ribosome determine tRNA kinetics. *J. Phys. Chem. B.* 121:10593–10601.
23. Nguyen, K., H. Yang, and P. C. Whitford. 2017. How the ribosomal A-site finger can lead to tRNA species-dependent dynamics. *J. Phys. Chem. B.* 121:2767–2775.
24. Whitford, P. C., J. K. Noel, ..., J. N. Onuchic. 2009. An all-atom structure-based potential for proteins: bridging minimal models with all-atom empirical forcefields. *Proteins.* 75:430–441.
25. Noel, J. K., M. Levi, ..., P. C. Whitford. 2016. SMOG 2: a versatile software package for generating structure-based models. *PLoS Comput. Biol.* 12:e1004794.
26. Delagoutte, B., D. Moras, and J. Cavarelli. 2000. tRNA aminoacylation by arginyl-tRNA synthetase: induced conformations during substrates binding. *EMBO J.* 19:5599–5610.
27. Silvyan, L. F., J. Wang, and T. A. Steitz. 1999. Insights into editing from an ile-tRNA synthetase structure with tRNA<sup>ile</sup> and mupirocin. *Science.* 285:1074–1077.
28. Shi, H., and P. B. Moore. 2000. The crystal structure of yeast phenylalanine tRNA at 1.93 Å resolution: a classic structure revisited. *RNA.* 6:1091–1105.
29. Kim, M., M. Wanunu, ..., A. Meller. 2006. Rapid fabrication of uniformly sized nanopores and nanopore arrays for parallel DNA analysis. *Adv. Mater.* 18:3149–3153.
30. Torrie, G., and J. Valleau. 1977. Nonphysical sampling distributions in Monte Carlo free-energy estimation: umbrella sampling. *J. Chem. Phys.* 23:187–199.
31. Hukushima, K., and K. Nemoto. 1996. Exchange Monte Carlo method and application to spin glass simulations. *J. Phys. Soc. Jpn.* 65:1604–1608.
32. Sugita, Y., and Y. Okamoto. 1999. Replica-exchange molecular dynamics method for protein folding. *Chem. Phys. Lett.* 314:141–151.
33. Hess, B., C. Kutzner, ..., E. Lindahl. 2008. GROMACS 4: algorithms for highly efficient, load-balanced, and scalable molecular simulation. *J. Chem. Theory Comput.* 4:435–447.
34. Yang, H., P. Bandarkar, ..., P. C. Whitford. 2019. Diffusion of tRNA inside the ribosome is position-dependent. *J. Chem. Phys.* 151:085102.
35. Crothers, D. M., P. E. Cole, ..., R. G. Shulman. 1974. The molecular mechanism of thermal unfolding of *Escherichia coli* formylmethionine transfer RNA. *J. Mol. Biol.* 87:63–88.
36. Kumar, S., J. M. Rosenberg, ..., P. A. Kollman. 1992. THE weighted histogram analysis method for free-energy calculations on biomolecules. I. The method. *J. Comput. Chem.* 13:1011–1021.
37. Jackson, J., K. Nguyen, and P. C. Whitford. 2015. Exploring the balance between folding and functional dynamics in proteins and RNA. *Int. J. Mol. Sci.* 16:6868–6889.
38. Whitford, P. C., P. Geggier, ..., K. Y. Sanbonmatsu. 2010. Accommodation of aminoacyl-tRNA into the ribosome involves reversible excursions along multiple pathways. *RNA.* 16:1196–1204.
39. Luan, B., and A. Aksimentiev. 2008. Electro-osmotic screening of the DNA charge in a nanopore. *Phys. Rev. E Stat. Nonlin. Soft Matter Phys.* 78:021912.
40. Luan, B., and A. Aksimentiev. 2010. Control and reversal of the electrophoretic force on DNA in a charged nanopore. *J. Phys. Condens. Matter.* 22:454123.
41. Zwanzig, R. 1988. Diffusion in a rough potential. *Proc. Natl. Acad. Sci. USA.* 85:2029–2030.
42. Bryngelson, J., and P. Wolynes. 1989. Intermediates and barrier crossing in A random energy-model (with applications to protein folding). *J Phys Chem-Us.* 93:6902–6915.
43. Hummer, G. 2005. Position-dependent diffusion coefficients and free energies from Bayesian analysis of equilibrium and replica molecular dynamics simulations. *New J. Phys.* 7:34.
44. Brune, D., and S. Kim. 1993. Predicting protein diffusion coefficients. *Proc. Natl. Acad. Sci. USA.* 90:3835–3839.
45. Gura Sadovsky, R., S. Brielle, ..., J. L. England. 2017. Measurement of rapid protein diffusion in the cytoplasm by photo-converted intensity profile expansion. *Cell Reports.* 18:2795–2806.
46. Alibakhshi, M. A., J. R. Halman, ..., M. Wanunu. 2017. Picomolar fingerprinting of nucleic acid nanoparticles using solid-state nanopores. *ACS Nano.* 11:9701–9710.
47. Chan, H. S., Z. Zhang, ..., Z. Liu. 2011. Cooperativity, local-nonlocal coupling, and nonnative interactions: principles of protein folding from coarse-grained models. *Annu. Rev. Phys. Chem.* 62:301–326.
48. Keyser, U. F., B. N. Koeleman, ..., C. Dekker. 2006. Direct force measurements on DNA in a solid-state nanopore. *Nat. Phys.* 2:473–477.
49. Ghosal, S. 2007. Electrokinetic-flow-induced viscous drag on a tethered DNA inside a nanopore. *Phys. Rev. E Stat. Nonlin. Soft Matter Phys.* 76:061916.
50. Harvey, S. C., and J. A. McCammon. 1981. Intramolecular flexibility in phenylalanine transfer RNA. *Nature.* 294:286–287.
51. Zhou, H. X., and K. A. Dill. 2001. Stabilization of proteins in confined spaces. *Biochemistry.* 40:11289–11293.
52. Klimov, D. K., D. Newfield, and D. Thirumalai. 2002. Simulations of  $\beta$ -hairpin folding confined to spherical pores using distributed computing. *Proc. Natl. Acad. Sci. USA.* 99:8019–8024.
53. O'Brien, E. P., G. Stan, ..., B. R. Brooks. 2008. Factors governing helix formation in peptides confined to carbon nanotubes. *Nano Lett.* 8:3702–3708.
54. Suvlu, D., S. Samaratunga, ..., J. C. Rasaiah. 2017. Thermodynamics of helix-coil transitions of polyalanine in open carbon nanotubes. *J. Phys. Chem. Lett.* 8:494–499.
55. Noel, J. K., P. C. Whitford, and J. N. Onuchic. 2012. The shadow map: a general contact definition for capturing the dynamics of biomolecular folding and function. *J. Phys. Chem. B.* 116:8692–8702.
56. Clementi, C., H. Nymeyer, and J. N. Onuchic. 2000. Topological and energetic factors: what determines the structural details of the transition state ensemble and “en-route” intermediates for protein folding? An investigation for small globular proteins. *J. Mol. Biol.* 298:937–953.
57. Hellinger, E. 1909. Neue Begründung der Theorie quadratischer Formen von unendlichvielen Veränderlichen. *J. Reine Angew. Math.* 136:210–271.
58. Whitford, P. C., and J. N. Onuchic. 2015. What protein folding teaches us about biological function and molecular machines. *Curr. Opin. Struct. Biol.* 30:57–62.